


## PAPER

Cite this: *Nanoscale*, 2020, **12**, 7146

## *In situ* TEM measurement of activation volume in ultrafine grained gold†

Saurabh Gupta,<sup>a</sup> Sandra Stangebye,<sup>a</sup> Katherine Jungjohann,<sup>b</sup> Brad Boyce,<sup>b</sup> Ting Zhu,<sup>a</sup> Josh Kacher<sup>a</sup> and Olivier N. Pierron<sup>b</sup>  <sup>\*,a</sup>

A micro-electromechanical system (MEMS) based technique is demonstrated for *in situ* transmission electron microscopy (TEM) measurements of stress relaxation with simultaneous observation of the underlying plastic deformation processes. True activation volumes are determined from repeated stress relaxation transients and thus provide a signature parameter of the governing mechanisms of plastic deformation. The technique is demonstrated with 100 nm-thick ultrafine-grained gold microspecimens under uniaxial tension. True activation volumes of approximately  $3-5b^3$  (where  $b$  is the Burgers vector length) are obtained for tensile stresses ranging from 200–450 MPa. Grain boundary-dislocation interactions are observed *via in situ* TEM during stress relaxation measurements. The miniaturization of stress relaxation tests inside the TEM provides unique opportunities to characterize the plastic kinetics and underlying mechanisms in ultrafine-grained and nanocrystalline materials.

Received 5th March 2020,  
Accepted 10th March 2020

DOI: 10.1039/d0nr01874k

rsc.li/nanoscale

### 1. Introduction

Plastic deformation properties of polycrystalline metals are known to be strongly affected by grain size, since decreasing grain size results in a higher volume fraction of grain boundaries (GBs) to impede dislocation glide.<sup>1–3</sup> Nanocrystalline (nc) and ultrafine grained (ufg) metals exhibit high strength<sup>4</sup> and high strain rate sensitivity,<sup>5</sup> but limited ductility.<sup>6</sup> Optimizing their mechanical properties for widespread applications<sup>7</sup> requires a thorough understanding of the underlying thermally activated plastic deformation mechanisms.<sup>8,9</sup> One of the main challenges associated with this grain size regime (<100 nm for nc, between 100 nm and 1  $\mu$ m for ufg) is the increasing role of GBs in mediating plastic deformation kinetics, and therefore the emergence of additional plastic deformation mechanisms related to the large volume fraction of GBs.<sup>9</sup> In pure coarse-grained face centered cubic (FCC) metals, room-temperature plasticity is carried out primarily by lattice dislocations that are generated or pre-exist in the grain interiors, and the strength is largely dominated by dislocation interaction with GBs, leading to the Hall–Petch effect.<sup>1–3</sup> Instead, in nc and ufg metals, lattice dislocations are mainly nucleated at the GBs since dislocation nucleation is con-

strained by the limited volume of the grain interior.<sup>10,11</sup> Moreover, deformation can induce numerous atomic defects within the GB, including GB extrinsic dislocations, (also known as disconnections)<sup>12–17</sup> which can move within the boundary itself, in part due to larger applied stresses. Hence a much richer picture exists for nc and ufg metals, with concurrent lattice dislocation and GB disconnection activities (and their interactions), leading to transgranular plasticity, grain rotation, grain growth, and GB sliding.<sup>15,18</sup> Atomistic simulations have been instrumental in investigating the mechanics of these defects, and have highlighted the challenges associated with understanding the effects of GB character<sup>18,19</sup> and triple junctions<sup>16,19–21</sup> on deformation mechanisms. Most studies have focused on bicrystals with symmetrical tilt GBs,<sup>12,13,17,22–24</sup> and there is still a significant gap in understanding for polycrystals (and the constraint effects of triple junctions) with more general GBs.<sup>15,16,25</sup>

Experimental characterization of defect mechanisms in real nc and ufg microstructures, having a wide range of GB characters and grain sizes, is an important step towards reducing this knowledge gap. *In situ* TEM experiments allow for the observation and characterization of active defect mechanisms<sup>26–31</sup> as well as the direct quantification of effects of some of these mechanisms (such as grain growth due to coupled GB shear and migration) when combined with automated crystal orientation mapping.<sup>26,32–34</sup> They can be naturally combined with atomistic simulations to study defect mechanics.<sup>35</sup> Given the inherent length and time scale limitations for each technique, *in situ* TEM and atomistic simulations can be more tightly integrated when mechanical pro-

<sup>a</sup>G. W. Woodruff School of Mechanical Engineering, Georgia Institute of Technology, Atlanta, GA 30332-0405, USA

<sup>b</sup>Sandia National Laboratories, P.O. Box 5800, Albuquerque, NM 87185, USA.

E-mail: olivier.pierron@me.gatech.edu

†Electronic supplementary information (ESI) available. See DOI: 10.1039/d0nr01874k

erties, such as stress and strain, are simultaneously measured. In this paper, we present a micro-electromechanical system (MEMS) with dimensions compatible with *in situ* TEM testing for the measurement of true activation volume,  $V^*$ . To the best of our knowledge, this is the first report of *in situ* TEM true activation volume measurements, thanks to the inherent stability of the MEMS device (compared to other existing quantitative *in situ* TEM techniques) that allows accurate measurements of successive, short stress relaxation segments. This parameter corresponds to the stress dependence of the activation energy of a mechanism, and is physically related to the number of atoms involved in overcoming the local energy barrier associated with the thermally activated mechanism.<sup>36</sup> It can therefore serve as a useful signature of the rate-controlling, plastic deformation mechanism.<sup>37</sup> Several studies on nc or ufg metals have used activation volume measurements, either at the macro-<sup>5,38,39</sup> or micro-scale,<sup>40,41</sup> in an effort to determine the governing mechanisms but without any *in situ* TEM observations. All these studies measured low activation volumes in the  $2\text{--}20b^3$  range, which are much smaller than the typical activation volumes exceeding  $250b^3$  for coarse-grained metals, thereby confirming the grain size effects on deformation mechanisms. However, some of these studies acknowledged the challenges of identifying the rate limiting processes solely based on activation volumes:<sup>39,42</sup> several mechanisms for nc-ufg metals may only differ by a small factor in activation volumes (say,  $10$  vs.  $20b^3$ ), the difference being of the same order as errors associated with assumptions in calculating that parameter. Clearly, performing *in situ* TEM observations of the plastic deformation mechanisms at the nanoscale while measuring  $V^*$  can alleviate these issues and provide more confidence that the observed mechanism is related to the measured  $V^*$ . In addition, true activation volume can also be obtained from atomistic reaction pathway simulations that do not suffer from the usual timescale limitations,<sup>4,43,44</sup> thereby providing further possible integration between experiments and simulations. Hence, we believe that our novel technique is a significant improvement over other quantitative *in situ* TEM techniques currently used to characterize plastic deformation mechanisms in nc and ufg materials. While the methodology of utilizing a MEMS device for *in situ* TEM nanomechanical testing has already been reported in our previous work,<sup>31,40,45–47</sup> here we report *in situ* TEM measurements of true activation volume on ufg Au microspecimens. Section 2 provides relevant details of the approach, while section 3 presents the measured activation volumes and observed plastic deformation mechanisms on 100 nm-thick ufg Au.

## 2. Experimental section

### 2.1. MEMS-based nanomechanical testing set-up

**2.1.1. Working principles of the MEMS device.** We have demonstrated the methodology to utilize a MEMS device for both *ex situ* and *in situ* TEM nanomechanical testing in our previous work.<sup>31,40,45–47</sup> A scanning electron microscopy (SEM)

image of the MEMS device is shown in Fig. 1(a) and its schematic illustration is shown in Fig. 1(b). The MEMS device consists of a thermal actuator, two interdigitated capacitive sensors (CS<sub>1</sub> and CS<sub>2</sub>), a load sensor (4 beams deforming in bending mode) and a “specimen gap” for allowing observations in the TEM. Non-conductive epoxy glue is used to connect different components of the system while still maintaining electrical isolation between them. Fig. 1(c) illustrates how the independent measurement of the change in capacitance in CS<sub>1</sub> and CS<sub>2</sub> allows the independent measurements of two displacements, one on each side of the specimen ( $X_A$  and  $X_{LS}$ ), which in turn provides stress and strain. The elongation of the specimen,  $X_S$ , is given by  $X_A - X_{LS}$ , from which strain is measured by dividing by the gauge section length. The force applied to the specimen (and therefore the stress by dividing by the cross-section area) can be calculated as  $K_{LS} \times X_{LS}$ , where  $K_{LS}$  is the load sensor stiffness (either 480 or 100 N m<sup>-1</sup> in this study).

**2.1.2. TEM set-up.** *In situ* TEM deformation experiments were performed in a FEI Tecnai F30 operating at 300 kV using two different electrical biasing holders: a Nanofactory Instruments holder (with 16 leads) used at the Center for Integrated Nanotechnologies (CINT), see Fig. 2(a), and a Hummingbird Scientific holder (with 8 leads) used at Georgia Tech (Fig. 2(b)). The Hummingbird chip carrier is made from printed circuit board (PCB); hence any exposed PCB material either on the front or the back side of the TEM holder can cause charging and astigmatism in the electron beam. Appropriate design of the chip carrier and use of silver paint to reduce the exposed PCB material was enough to reduce drift associated with charging (measured to be below 5 nm min<sup>-1</sup>).

**2.1.3. Capacitive sensing and CS<sub>1</sub> and CS<sub>2</sub> calibration.** The displacement of the capacitive sensors  $X$  can be related to their change in capacitance  $\Delta C$  using:

$$\Delta C = \alpha \epsilon_0 n A \left[ \left( \frac{1}{d_1 - X} + \frac{1}{d_2 + X} \right) - \left( \frac{1}{d_1} + \frac{1}{d_2} \right) \right] \quad (1)$$

where  $\alpha$  is the calibration constant,  $\epsilon_0 = 8.854 \times 10^{-12}$  Fm<sup>-1</sup> is the permittivity of free space,  $n = 42$  is the number of comb structures,  $A$  is the overlapping area of the comb structure,  $d_1$  (nominal value: 2.5  $\mu$ m) and  $d_2$  (nominal value: 10.5  $\mu$ m) are the initial gaps between the comb structures which are measured using SEM images of the device typically before or after the test.

The change in capacitance  $\Delta C$  of sensors CS<sub>1</sub> and CS<sub>2</sub> is measured using a commercially available CMOS chip MS3110. This chip measures the difference between two input capacitances and provides an output voltage  $V_{\text{out}}$  proportional to the difference. To measure the value of one capacitive sensor alone (say CS<sub>1</sub> or CS<sub>2</sub>), one can measure the difference between CS<sub>1</sub> (or CS<sub>2</sub>) and a constant capacitor (see ref. 47 for details).  $\Delta CS_1$  (or  $\Delta CS_2$ ) as a function of  $V_{\text{in}}$  is then given by:

$$\Delta CS_1 = \left[ \overline{V_{\text{out}}^a}(V_{\text{in}} = 0) - \overline{V_{\text{out}}^a}(V_{\text{in}}) \right] / \lambda^a \quad (2)$$

$$\Delta CS_2 = \left[ \overline{V_{\text{out}}^b}(V_{\text{in}} = 0) - \overline{V_{\text{out}}^b}(V_{\text{in}}) \right] / \lambda^b \quad (3)$$

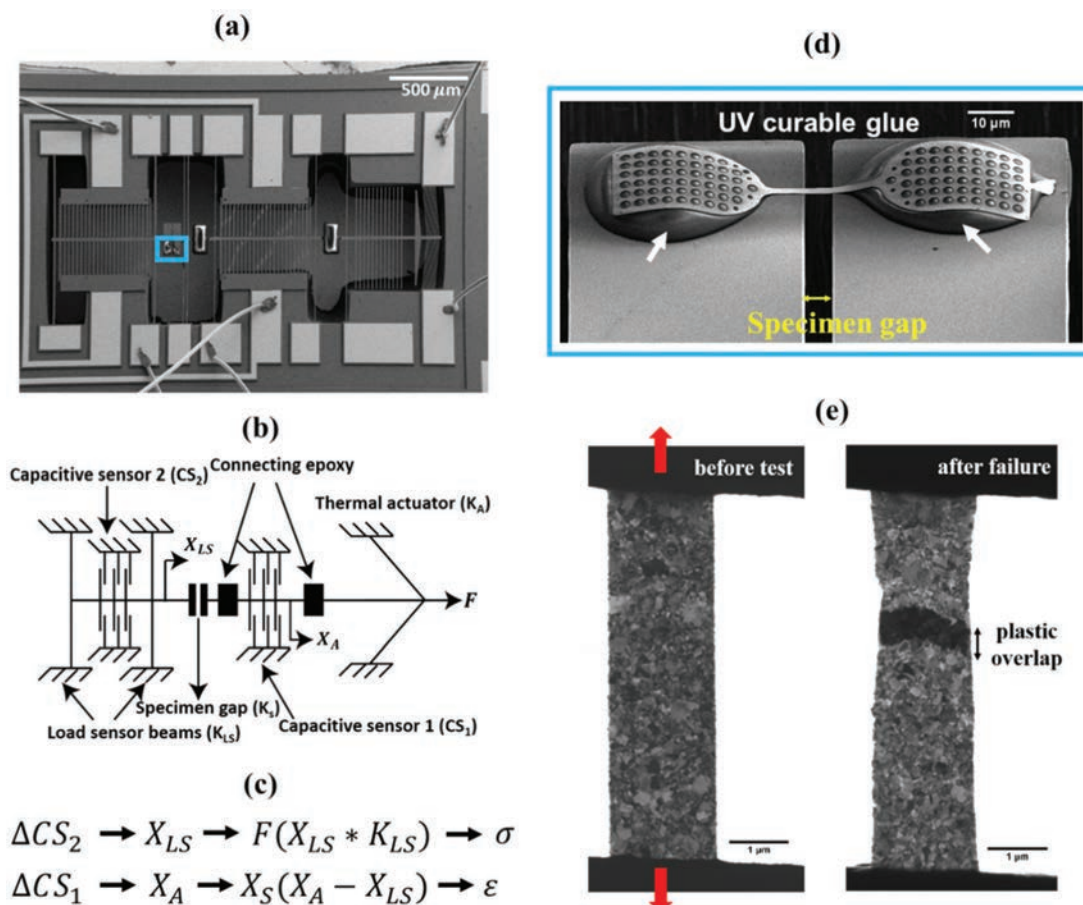


Fig. 1 (a) SEM image of the MEMS device. (b) Schematic of the MEMS device. (c) Calculation of  $\sigma$  and  $\epsilon$  from the measured capacitive displacements. (d) Inclined SEM image of an untested microspecimen manipulated without using FIB. (e) TEM images showing a microspecimen before and after testing.

where the superscripts  $a$  and  $b$  refer to the two MS3110s respectively,  $\lambda^a$  and  $\lambda^b$  are the proportionality constants of the two MS3110s.  $\overline{V_{out}}$  represents the average of a block of samples of  $V_{out}$  collected over  $\sim 1$  s, sampled at 1–5 kHz by the data acquisition unit. For our *in situ* experiments performed with the holders mentioned in section 2.1.2, the noise level in  $\overline{V_{out}}$  is low, typically around 50 mV, leading to noise levels of 0.1–0.2 fF in capacitance, and ultimately a precision of 1–2 MPa in stress.

The calibration constant,  $\alpha$  in eqn (1) accounts for the deviation of the capacitances measured by the capacitive sensors from the analytical equation and is assumed to be a constant for the entire duration of a test. It is obtained separately for each of the two MS3110s used to measure  $\Delta CS_1$  and  $\Delta CS_2$ . To calculate  $\alpha_{CS_1}$  ( $\alpha$  associated with the MS3110 chip measuring  $\Delta CS_1$ ), a series of  $X_A$  values are measured *in situ* via TEM at different  $V_{in}$  values and the corresponding  $(\Delta CS_1)_{exp}$  values are simultaneously measured *via* the MS3110 chip. Using the  $X_A$  values, eqn (1) is fitted to the experimentally measured  $(\Delta CS_1)_{exp}$  values to obtain  $\alpha_{CS_1}$ . Similarly,  $\alpha_{CS_2}$  is calculated by measuring  $X_{LS}$  *via* TEM and the corresponding  $(\Delta CS_2)_{exp}$ . Therefore, the two constants  $\alpha_{CS_1}$  and  $\alpha_{CS_2}$  can be measured

independently in the TEM, which is a more robust calibration scheme than what was previously used for *ex situ* tests.<sup>47</sup>

## 2.2. Specimen manipulation: effect of pre-stress on the $\sigma$ – $\epsilon$ curve

The specimens used in this study were fabricated independent of the MEMS device using a process involving optical lithography, electron-beam evaporation, a lift-off technique, and XeF<sub>2</sub> etching of the Si substrate with a thin native oxide; details of the procedure can be found in ref. 31. At the end of the process, the specimens are free-standing cantilevers, connected on one side to a large island as a support. In order to test these free-standing specimens, we have developed a FIB-less specimen manipulation procedure detailed in ref. 40. Fig. 3(a) shows the monotonic stress–strain behavior of an Au sample tested *in situ*, with an apparent anomaly of a negative stress (about –80 MPa) after failure. TEM imaging of the CS<sub>2</sub> gap before and after testing showed that the initial gap (with untested specimen at  $V_{in} = 0$ ) was 2.77  $\mu\text{m}$  and the gap increased to 2.80  $\mu\text{m}$  after the microspecimen failed, indicating that CS<sub>2</sub> was initially (before the test) under a positive stress equivalent to 30 nm of  $X_{LS}$ . This corresponds to a pre-

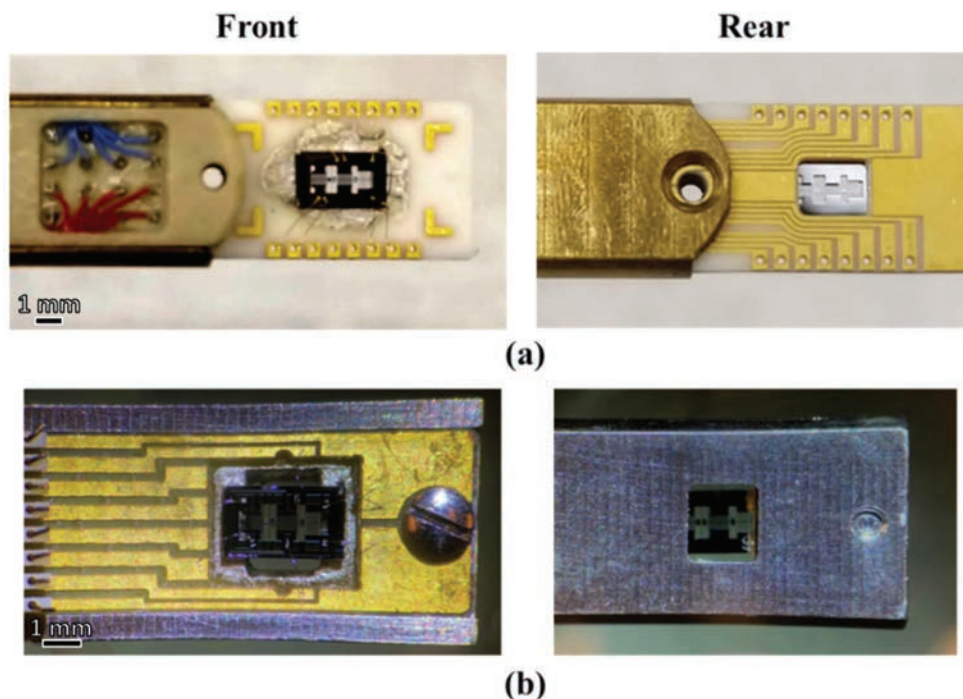


Fig. 2 (a) Nanofactory Instruments chip carrier design used at CINT. (b) Chip carrier by Hummingbird Scientific used at Georgia Tech.

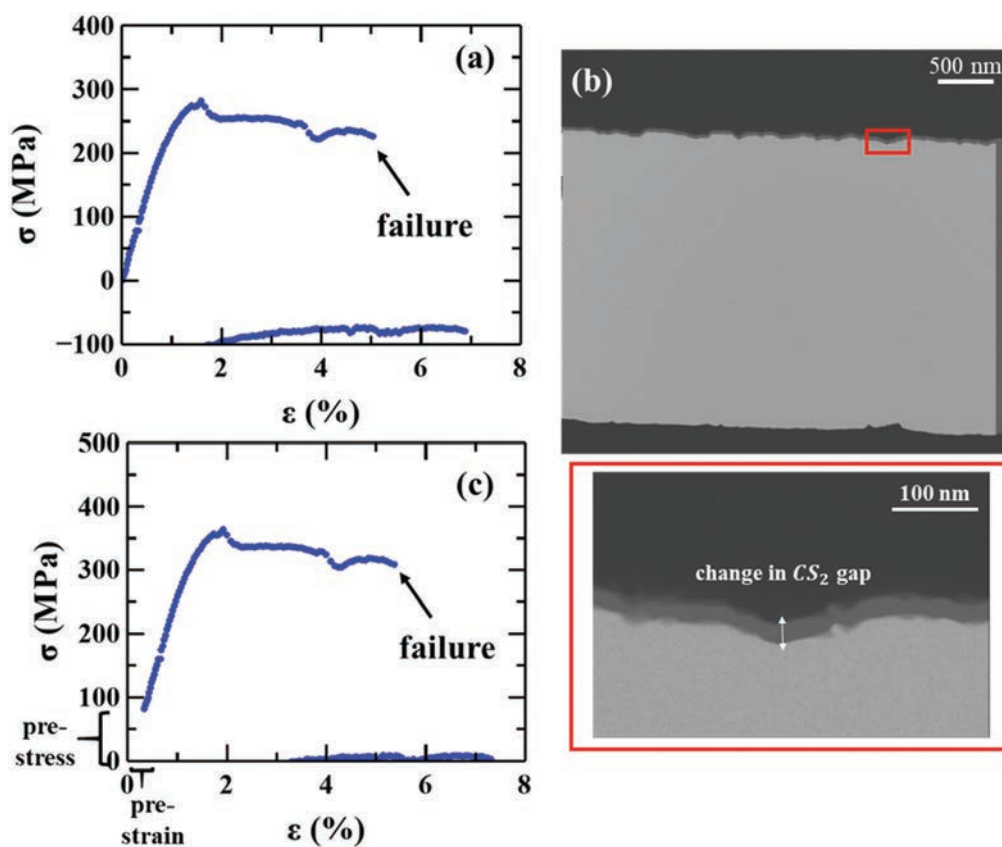


Fig. 3 (a) Monotonic  $\sigma$ - $\epsilon$  curve of 100 nm-thick Au microspecimen showing a negative stress of  $-80$  MPa after failure instead of zero. (b) Overlay of the TEM images of the  $CS_2$  gap before test and after microspecimen failure showing a difference of 30 nm in the gap indicating the existence of a tensile pre-stress of 82 MPa (see text) in the microspecimen. (c) Stress-strain curve corrected for pre-stress, showing normal behavior (no stress after failure).



stress value of 82 MPa. This pre-stress arises from the UV curable glue used to attach the samples to the MEMS device. Upon curing, the glue shrinks causing an elongation in the specimen and a resulting displacement in  $X_{LS}$ . This ultimately results in a small amount of elastic strain in the specimen. As shown in Fig. 3(c) and based on our TEM observations, no significant plastic deformation occurs due to this pre-load. Accounting for this pre-stress and strain, the updated  $\sigma$ - $\epsilon$  curve (see Fig. 3(c)) shows a normal behavior with no measured stress after failure. Hence the accuracy in stress measurement is demonstrated, by accounting for pre-stress and performing the calibration discussed earlier.

### 2.3. Definition and calculation of true activation volume

The true activation volume  $V^*$  can be measured by performing repeated stress relaxations, with an elastic reloading between two consecutive stress relaxation tests.<sup>36</sup> It is given by:

$$V^* = kT \frac{\ln(\dot{\gamma}_{i2}/\dot{\gamma}_{f1})}{\Delta\tau_{12}} = \sqrt{3}kT \frac{\ln(\dot{\epsilon}_{i2}/\dot{\epsilon}_{f1})}{\Delta\sigma_{12}} \quad (4)$$

where  $k$  is the Boltzmann constant,  $T$  is the temperature in Kelvin,  $\dot{\gamma}_{i2}$  is the plastic shear strain rate at the start of the second relaxation,  $\dot{\gamma}_{f1}$  is the plastic shear strain rate at the end of the first relaxation,  $\Delta\tau_{12}$  is the increase of shear stress during reloading;  $\dot{\epsilon}_{i2}$ ,  $\dot{\epsilon}_{f1}$  and  $\Delta\sigma_{12}$  are the corresponding normal strain and stress components. The plastic strain rates are measured by fitting the stress relaxation data using a logarithmic function.<sup>40,47</sup> It is noted that the true activation volume defined in eqn (4) (also called physical activation volume) contrasts with the apparent activation volume  $V_a$  that can be also determined from stress relaxation test according to:

$$V_a = -\frac{kT \ln(1 + t/c_\tau)}{\Delta\tau} = -\frac{\sqrt{3}kT \ln(1 + t/c_\tau)}{\Delta\sigma} \quad (5)$$

where  $c_\tau$  is time constant and  $\Delta\tau$  is the decrease in stress during a relaxation. The true activation volume  $V^*$  character-

izes the stress sensitivity of dislocation velocity, while the apparent activation volume  $V_a$  is additionally accompanied with a change of mobile dislocation density.<sup>5,36,39,48,49</sup> In this work, we focus on the measurement of true activation volume, which represents the direct stress effect on dislocation velocity and thus is closely linked to the rate-controlling dislocation processes. As a reference, the apparent activation volume is also measured and is typically greater than the true activation volume due to relaxation of mobile dislocations. In addition, the stress rates are obtained by fitting the stress relaxation data and can be converted to plastic strain rates<sup>40</sup> by:

$$\dot{\epsilon}_p = -\dot{\sigma}/M \quad (6)$$

where  $M$  is the machine-specimen stiffness.<sup>31,40,47</sup>

The apparent activation volume  $V_a$  can also be related to the strain rate sensitivity  $m$  by:

$$m = \sqrt{3}kT/\sigma V_a \quad (7)$$

### 2.4. Accuracy of activation volume measurements

Using eqn (6), eqn (4) can be re-written as follows:

$$V^* = \sqrt{3}kT \frac{\ln(\dot{\epsilon}_{i2}/\dot{\epsilon}_{f1})}{\Delta\sigma_{12}} = \sqrt{3}kT \frac{\ln(\dot{\sigma}_{i2}/\dot{\sigma}_{f1})}{\Delta\sigma_{12}} \quad (8)$$

Eqn (8) shows that the accuracy of the true activation volume measurement depends on the accuracy of measurement of the plastic strain rates  $\dot{\epsilon}$  (or the stress decrease rates  $\dot{\sigma}$ ) and the stress decrease  $\Delta\sigma$ , and is independent of the gauge length or the absolute value of  $\sigma$  or  $\epsilon$ . The accuracy in the determination of these rates depends largely on the quality of the logarithmic fit to the stress relaxation data, and therefore is affected significantly by the signal-to-noise ratio (SNR) of the measurement. In order to calculate SNR for a stress relaxation segment, the amount of stress relaxation  $\Delta\sigma$  and the noise  $\delta\sigma$  needs to be calculated. SNR is then given by:

$$\text{SNR} = \Delta\sigma/|\delta\sigma| \quad (9)$$

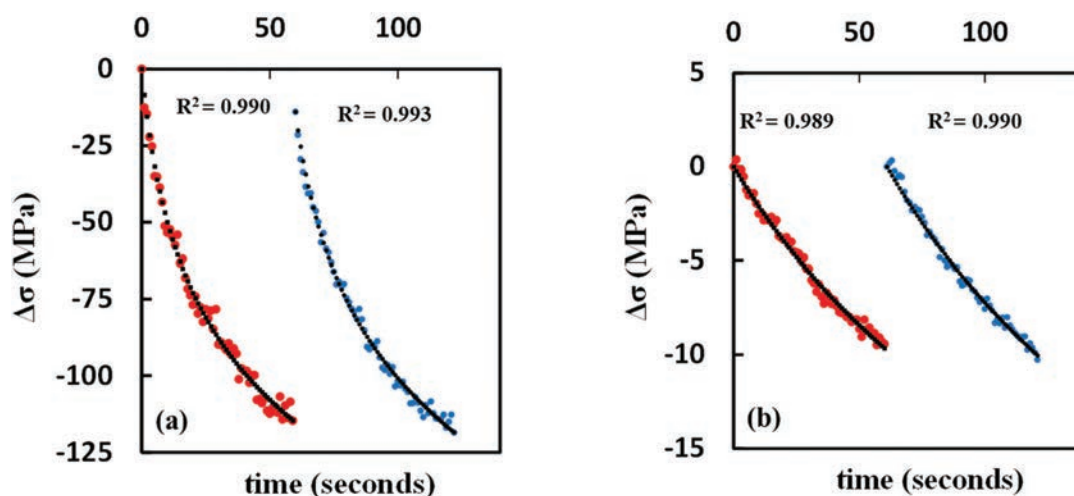


Fig. 4 Examples of logarithmic fits with  $R^2$  greater than 0.90: (a)  $\Delta\sigma = 110$  MPa,  $\delta\sigma = \pm 2$  MPa (SNR = 25). (b)  $\Delta\sigma = 10$  MPa,  $\delta\sigma = \pm 0.3$  MPa (SNR = 16.6).

To calculate  $\Delta\sigma$  and  $\delta\sigma$  for a relaxation segment, the best logarithmic fit to relaxation segment is determined.  $\Delta\sigma$  is then given by the difference between the initial and final values of  $\sigma$  during the relaxation.  $|\delta\sigma|$  is given by twice the standard deviation of the difference between the actual data and the fit.

Fig. 4(a) and (b) show examples of stress relaxation segments with SNR values of 25 and 16.6 respectively. The corresponding logarithmic fits of the stress relaxations are associated with large  $R^2$  values (around 0.99). For our measurements, we only use logarithmic fits with  $R^2$  values greater than 0.90 to calculate accurate  $V^*$  measurements, which correspond to SNR values above 5. Given our noise level for  $\delta\sigma$  of  $\pm 2$  MPa, our *in situ* TEM activation volume measurements require  $\Delta\sigma$  to exceed 10 MPa, meaning our current approach (60 s relaxation segments) can be used to characterize mechanisms associated

with low or medium  $V^*$ . For large  $V^*$  ( $>100b^3$ ),  $\Delta\sigma$  may not exceed 10 MPa within 60 s relaxation segments. Longer relaxation segments may provide large enough signal ( $\Delta\sigma$ ) to accurately calculate  $V^*$ , although such measurements have not been performed.

### 3. Results and discussion

#### 3.1. Microstructure of 100 nm-thick Au microspecimens

The SEM images of the free-standing Au microspecimens are shown in Fig. 5(a) and (b). The nominal gauge length of these specimens is 20  $\mu\text{m}$ , width is 1.8  $\mu\text{m}$  and thickness is 100 nm. It can be seen in Fig. 5(b) that there are a few large grains  $\sim 300\text{--}400$  nm in size among many small grains  $<100$  nm in

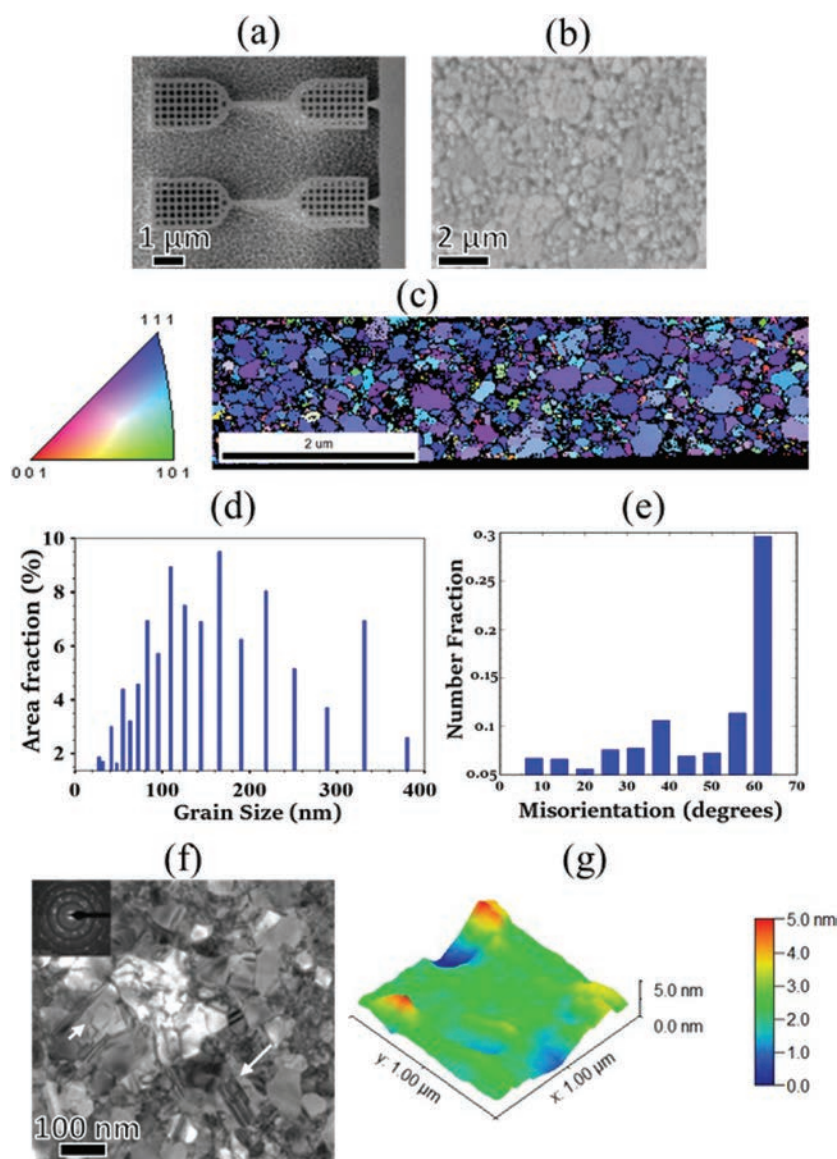


**Fig. 5** Microstructural characterization of 100 nm-thick Au ultrathin microspecimens. (a) and (b) SEM images of the free-standing microspecimens. (c) TKD map of the gauge length showing  $\langle 111 \rangle$  out-of-plane texture. (d) Area fraction grain size distribution. (e) Grain boundary misorientation distribution. (f) TEM image of the film showing twins and dislocations within the grains, indicated by arrows. (g) AFM map of the surface roughness.

size. Fig. 5(c) shows a Transmission Kikuchi Diffraction (TKD)<sup>50</sup> map of the microspecimen which clearly reveals a  $\langle 111 \rangle$  out-of-plane texture, as is commonly observed in deposited Au films.<sup>51,52</sup> The grain size distribution obtained from the TKD map quantitatively shows the distribution of large and small grains, with an average grain size calculated to be 150 nm (Fig. 5(d)). The grain boundary misorientation, shown in Fig. 5(e), obtained from the TKD map indicates that the micro-specimen contains a high percentage of high angle grain boundaries (HAGBs) with misorientations greater than  $15^\circ$ . Thirty percent of the grain boundaries have a misorientation of  $60^\circ$  and correspond to  $\Sigma 3$  twin boundaries. Fig. 5(f) shows a TEM image of the ultrathin microspecimen. Twins and dislocations can be seen within some of the grains and the diffraction pattern in the inset shows no in-plane texture. The atomic force microscopy (AFM) map of the surface roughness of these microspecimens shown in Fig. 5(g) reveals that the average surface roughness of these microspecimens is 1.5 nm ( $\sim 1.5\%$  of the thickness). However, there are some larger grooves,  $\sim 5$  nm deep, which can influence the mechanical properties of these ultrathin microspecimens.

### 3.2. *In situ* TEM tensile behavior

Fig. 6 shows the results of an *in situ* TEM tensile test to failure performed at low magnification in order to demonstrate the technique and highlight the global deformation behavior and mechanical response of our 100 nm-thick Au microspecimens. The test was conducted at a strain rate of  $\sim 1\text{--}2 \times 10^{-4} \text{ s}^{-1}$ . Fig. 6(a)–(f) show snapshots from the bright field TEM recording, while Fig. 6(g) shows the measured stress–strain curve (accounting for pre-stress). Some of the TEM snapshots are superposed by local strain measurements based on markers identified on the edges of the specimen that were tracked during the test. The markers define sub-regions of the sample; these sub-regions are identified by rectangles in the image, with the color of the rectangle indicating the local strain level. The 0.2%-offset yield stress is 450 MPa, and the tensile strength is 460 MPa. Microplasticity develops up to 1.5% strain, after which the stress remains constant up to 2.5% strain. This is confirmed with the local strain measurements showing strain localization in the top portion of the specimen at 3.6% strain (see Fig. 6(c)). Deformation localizes in that region, with formation of a neck in the width direction (see Fig. 6(d) at 4.2% strain) followed by crack formation and propagation. Final failure occurs along a plane at approximately  $45^\circ$  to the tensile axis (see Fig. 6(f)). Based on these results, activation volume measurements can be performed over the first 1–2% of plastic strain, before necking occurs.<sup>37</sup>

### 3.3. *In situ* TEM measurement of true activation volume

Stress relaxation experiments were performed on the Au microspecimens with *in situ* TEM observations. Repeated stress relaxation tests consisted of consecutive 30–60 seconds long stress relaxation segments, with each relaxation segment starting at approximately at the same stress. Although the length of the relaxation segments was nominally around 30 seconds for

most of our previous *ex situ* experiments,<sup>40</sup> this duration was increased to 60–120 seconds for *in situ* experiments to increase the accuracy of the measurements. Apart from these short transients, transients up to 20 minutes long were needed for TEM observations and the defect behavior.

Fig. 7 shows transient repeated stress relaxations of 100 nm-thick Au microspecimens. In Fig. 7(a), we plot the stress–strain curve corresponding to the complete test including these stress transients. The stress transients are straight lines with a negative slope on the graph. Fig. 7(b) shows the individual relaxation segments, each of which are 60 seconds long. The magnitude of the stress relaxation,  $\Delta\sigma$ , varies strongly with the stress level at the start of the stress relaxation,  $\sigma_i$ . When  $\sigma_i$  is around 250–300 MPa,  $\Delta\sigma$  associated with each transient is approximately 20 MPa. For  $\sigma_i$  values around 450 MPa, the  $\Delta\sigma$  is around 100 MPa ( $\sim 25\%$  of  $\sigma_i$ ). As shown in Fig. 7(c) and (d),  $V^*$  ranges from 3 to  $5b^3$  ( $b = 0.288$  nm for Au) for these transients. The strain rate sensitivity  $m$  is  $\sim 0.1$  and the apparent activation volume  $V_a$  is between  $5\text{--}30b^3$  as seen in Fig. 7(e) and (f) respectively.

### 3.4. *In situ* TEM observations

Fig. 7 shows an example of an *in situ* TEM test consisting of several series of short ( $\sim 60$  s) stress relaxation segments in order to measure  $V^*$  as a function of stress (Fig. 7(c)) and plastic strain (Fig. 7(d)). Alternatively, we performed multiple experiments consisting of loading a specimen to a certain level of deformation, at which point  $V^*$  was measured (applying two short relaxation segments). After that measurement, a longer (up to 20 min) relaxation segment was applied for TEM observations at higher magnifications of operating plastic deformation mechanisms. The observed area is  $\sim 0.5\text{--}1 \mu\text{m}^2$  and represents 5–10% of the total area of the specimen's gauge section. Following these observations, the test can be either interrupted or continued at larger deformations. Since plastic deformation accumulates during the long relaxation segments, the reported strain values can be larger than that of Fig. 7. Below are examples of several tests on different specimens, for which the measured  $V^*$  ranged from 3 to  $6b^3$ .

Early in deformation, isolated dislocation nucleation and interactions of both perfect and partial dislocations are observed. An example of partial dislocation activity can be seen in Fig. 8 (see Movie 1 in ESI†), where a single partial dislocation is emitted from a GB, resulting in a stacking fault region within the grain (marked by arrowhead). After four seconds, the trailing partial dislocation is emitted; and the full dislocation traverse through the grain and is absorbed by the opposite GB. The snapshots were taken at  $\sigma \sim 170$  MPa and  $\epsilon \sim 3.2\%$ .

An example of isolated perfect dislocation nucleation is shown in Fig. 9 (see Movie 2 in ESI†). These images were captured during two consecutive stress relaxation segments starting at  $\sigma = 230$  MPa. Fig. 9(b) shows a dislocation loop originating at a triple junction (indicated by arrowhead) in the middle of the first relaxation at  $\sigma \sim 215$  MPa and  $\epsilon \sim 5.1\%$ . Over the next four and half minutes the dislocation loop grows and tra-

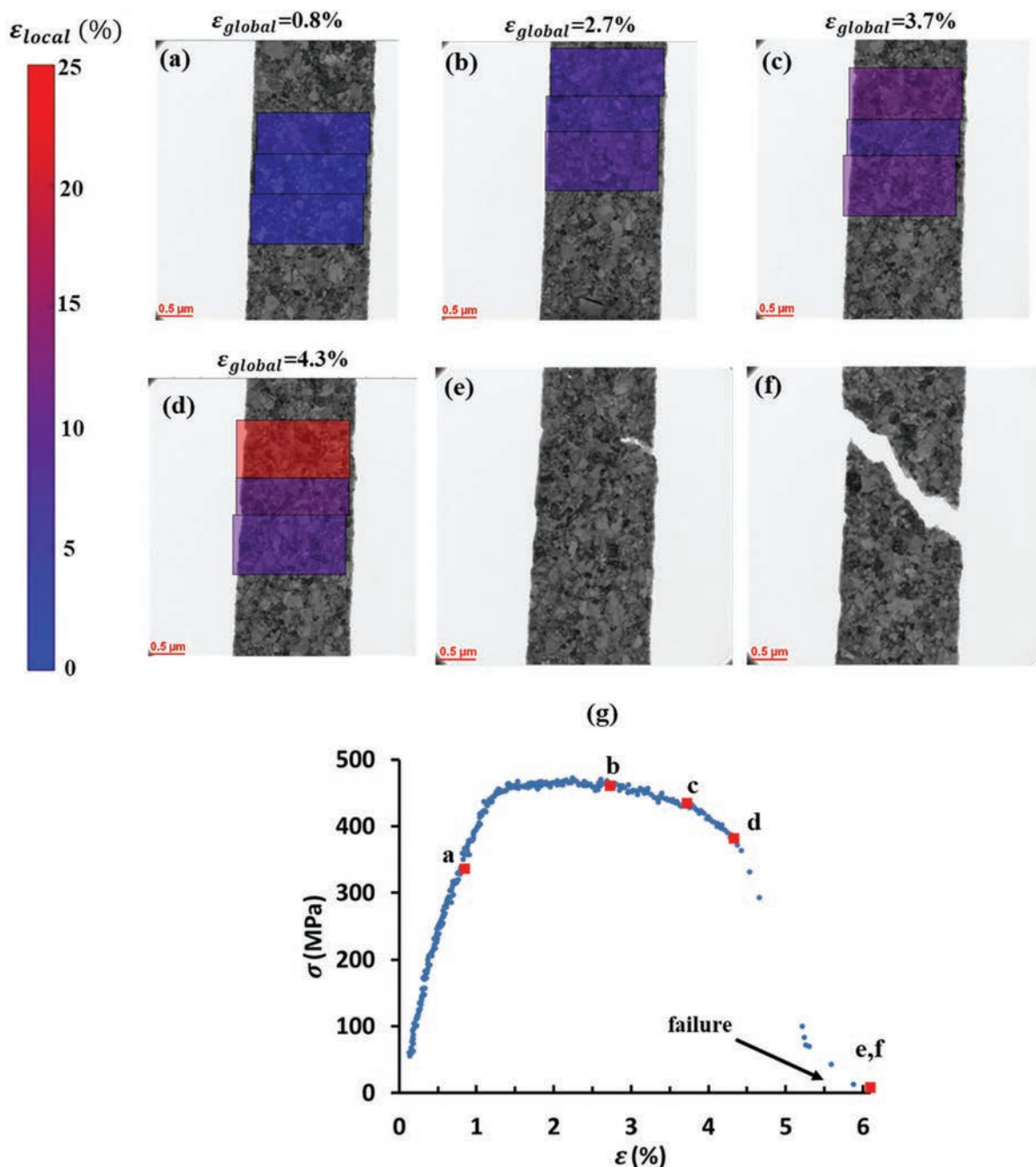


**Fig. 6** *In situ* TEM monotonic testing of a 100 nm-thick Au microspecimen. Local strain distributions in three regions namely top, middle and bottom are shown in (a)–(d) computed by DIC at instances indicated on the stress–strain curve in (g). (e) and (f) TEM snapshots near complete failure of the microspecimen.

verses through the grain (shown by arrowheads) and ultimately exits the crystal (see Fig. 9(b)–(g)). An important feature of this dislocation behavior is that the pinning points of the dislocation loop are always at the GBs, reflecting the fact that the density of dislocation interlocks is not as high as in conventional coarse-grained metals and the GBs therefore act as the major pinning points. Dupraz *et al.*<sup>53</sup> have shown similar mechanisms through molecular dynamics simulation on nc Al. They showed that the dislocations are pinned at the triple

junctions and grain boundary ledges. They associated the propagation of the dislocations to depinning of the dislocations and nucleation of a partial dislocation.

Another dislocation mechanism observed is dislocation cross-slip leading to a transition between intra- to intergranular glide. An example of this can be seen in Fig. 10 (see Movie 3 in ESI†), where a single dislocation (marked by arrowhead) cross-slips onto a boundary plane. The boundary plane is presumably a coherent twin boundary, though this could not be



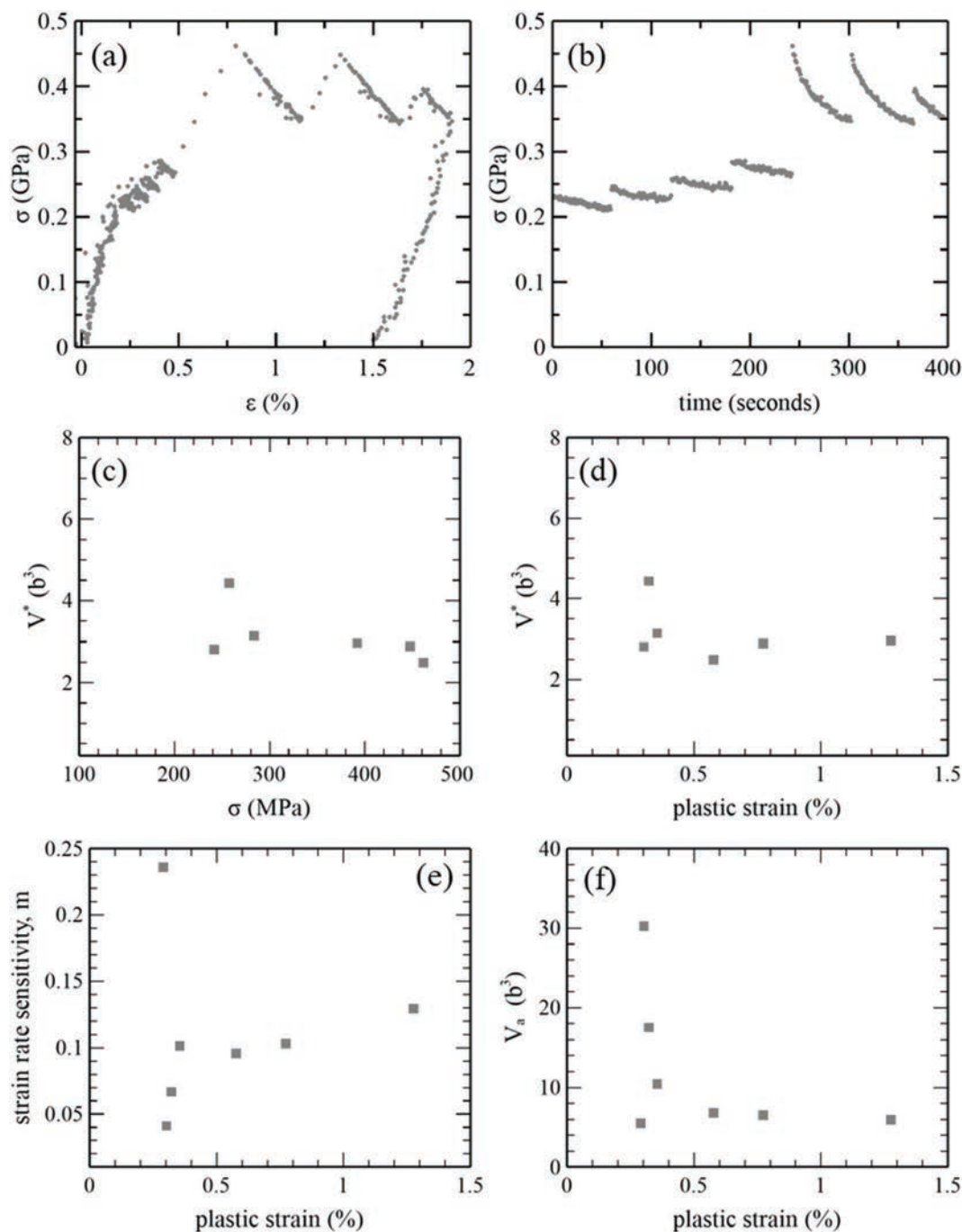


Fig. 7 *In situ* TEM repeated stress relaxations of a 100 nm-thick Au microspecimen. (a) Stress–strain evolution during the test. (b) Stress relaxation segments. (c) and (d) Corresponding  $V^*$  versus stress and plastic strain, respectively. (e) and (f) Corresponding  $m$  and  $V_a$  values, respectively.

confirmed during the *in situ* experiment. In Fig. 10(d), the dislocation can be seen gliding in the boundary plane after cross-slip has occurred.

In the late stages of deformation, multiple slip systems are activated. An example showing this is presented in Fig. 11 (see Movie 4 in ESI†), where many dislocations are seen within a single grain. These snapshots occurred one minute into a relaxation segment, with  $\sigma \sim 216$  MPa and  $\epsilon \sim 7.1\%$ .

### 3.5. Discussion and outlook

The experiments shown in sections 3.3 and 3.4 are, to the best of our knowledge, the first quantitative *in situ* TEM measurements of  $V^*$  in ufg metals, using Au thin film microspecimens. It should be noted that, in these experiments, the measured  $V^*$  value is not necessarily associated with the observed mechanism; instead, it is associated with the governing mechanism

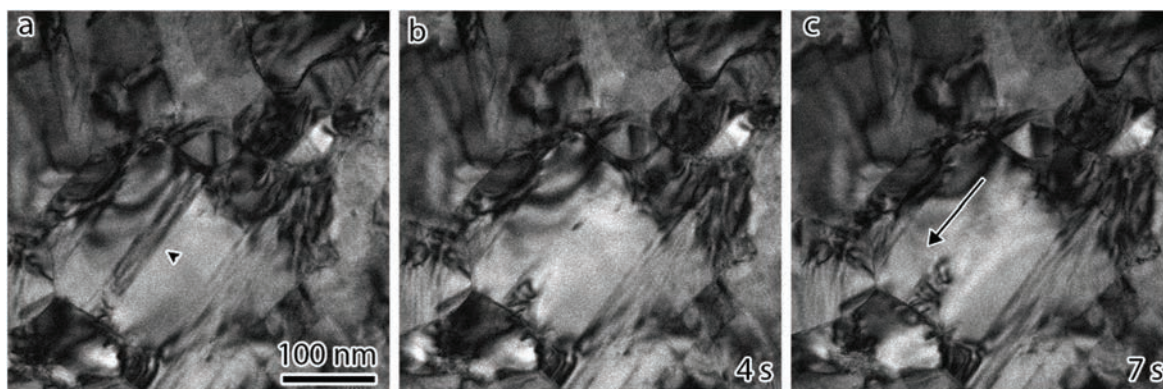


**Fig. 8** Emission of the leading and trailing partial dislocation from a GB during a stress relaxation segment (a–c). Arrowhead in (a) indicates the stacking fault region between leading and trailing partial dislocations, and arrow in (c) indicates direction of dislocation glide.

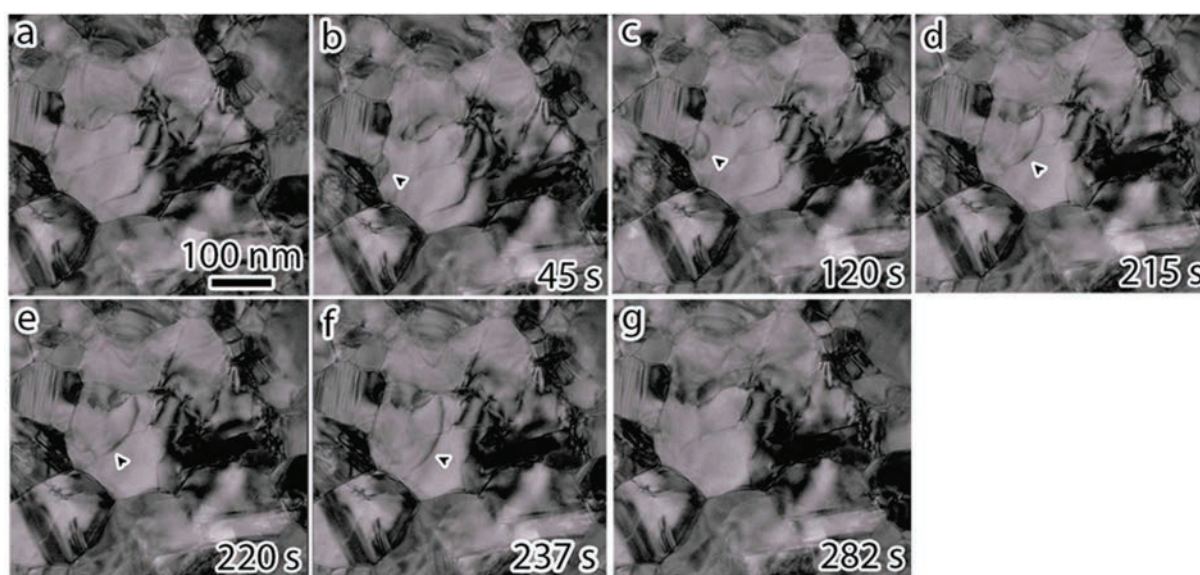


**Fig. 9** Frames from *in situ* TEM video showing dislocation nucleation from a triple junction and traversing through a grain during a relaxation segment. The dislocation of interest is marked by an arrowhead in (b–f). The dislocation was absorbed into a grain boundary between frames (f) and (g). Experiment time with respect to frame (a) is given in each frame.

dictating the overall response of the specimen. As mentioned in the introduction and illustrated in 3.4, several plastic deformation mechanisms can be active in nc and ufg metals. Hence, TEM observations provide a list of candidate governing mechanisms, and our novel technique can be used to determine which of these candidates is the governing mechanism. To that end, atomistic reaction pathway simulations of activation volumes of dislocation processes as well as dislocation-GB interactions can be used for direct comparison with our *in situ* TEM experiments. One of the main advantages of these simulations is that it does not suffer from the timescale limitation of molecular dynamics.<sup>4,43,44</sup> Hence, these atomistic simulations can model unit dislocation processes that are consistent with *in situ* TEM observations and provide a simulated  $V^*$  for each observed mechanism. The mechanism for which the simulated  $V^*$  is close to the measured  $V^*$  is likely the rate-

controlling mechanism. Our coupled *in situ* TEM stress relaxation experiments and atomistic reaction pathway simulations are underway and will be reported in future publications.

The measured  $V^*$  values shown in section 3.3 and 3.4 are very similar to the *ex situ*  $V^*$  measurements that were previously performed (also ranging from  $\sim 3$  to  $5b^3$ ).<sup>40</sup> This suggests that the electron beam irradiation in our experiments has a negligible effect on the governing plastic deformation mechanisms of our Au specimens. Indeed, recent quantitative *in situ* TEM studies have highlighted unexpected effects of the electron beam (under certain configurations) on the mechanical properties of small volume specimens.<sup>54,55</sup> More specifically, Li *et al.*<sup>54</sup> have proposed that the electron beam irradiation can trigger plastic deformation dominated by interface dislocation nucleation as a result of its effect on the native oxide of Al-4Cu alloy microspecimens. This electron beam arti-



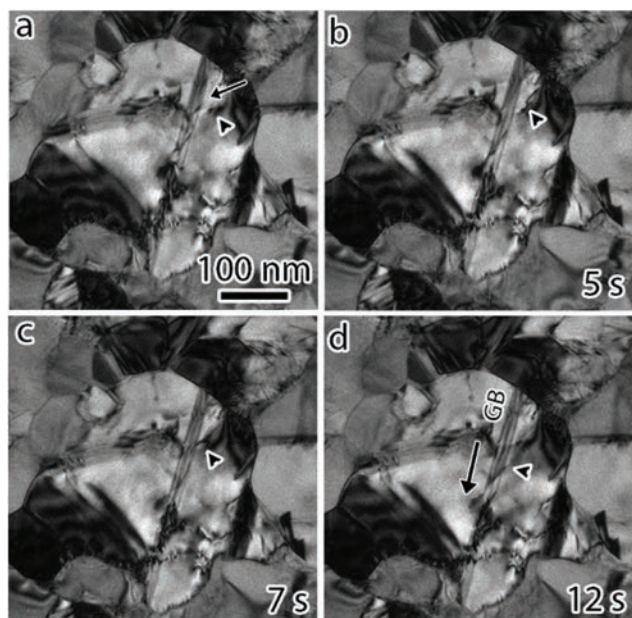


**Fig. 10** (a)–(d) Frames from *in situ* TEM video showing dislocation cross-slip and subsequent intergranular glide along boundary plane during stress relaxation. Arrows in (a) and (b) indicate direction of dislocation glide and the arrowhead in each frame track a single dislocation as it cross slips and glides in the boundary. Experiment time is given in each frame.

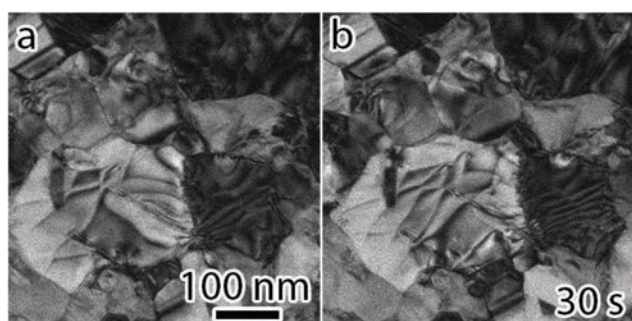


**Fig. 11** (a) and (b) TEM micrograph of dislocations on multiple slip systems during late stage deformation. Time elapsed between micrographs is given in (b).

fact is unlikely to occur with noble metals such as Au as they do not form native oxides.

We compare our results to recent studies on free-standing Au thin films in order to highlight the added benefit of our approach. Merle *et al.* investigated the time-dependent inelastic properties of ufg Au thin films with similar microstructures (median grain size ranging from 100 to 300 nm, thickness ranging 200 to 400 nm, strong  $\langle 111 \rangle$  out-of-plane texture), using bulge tests.<sup>56</sup> They measured  $m$  values on the order of 0.1 for strain rates around  $10^{-5} \text{ s}^{-1}$ , in good agreement with our results (see Fig. 7(e)). They acknowledged that gaining insight into the governing plastic deformation mechanisms solely based on  $m$  values is challenging and suggest that dis-

location glide mechanisms are more likely to govern plastic deformation than mechanisms such as diffusion-based GB sliding for which larger  $m$  values ( $\sim 0.5$ ) are typically obtained. In contrast, our *in situ* TEM technique not only measures similar  $m$  values (in addition to measuring  $V^*$ ) but also provides unambiguous proof that transgranular and intragranular dislocation activities indeed operate in this regime, along with key details about the observed GB/dislocation interactions.

Jonnalagadda *et al.* also investigated the plastic deformation behavior of nc Au thin films,<sup>52</sup> with also a strong  $\langle 111 \rangle$  out-of-plane texture, but with average grain sizes of 38 and 44 nm (as opposed to 150 nm in this study), and a much narrower grain size distribution. They used a microtensile technique coupled with digital image correlation to apply strain rates ranging from  $6 \times 10^{-6}$  to  $20 \text{ s}^{-1}$ , from which they can measure  $m$  and  $V_a$  (see eqn (7)). They measured a 0.2% yield stress of around 700 MPa at a strain rate of  $10^{-4} \text{ s}^{-1}$ , while our yield stress is 450 MPa at that strain rate. This difference can be explained by the Hall–Petch effect, given our larger average grain size of  $\sim 150 \text{ nm}$ . They observed a decrease in  $V_a$  (from  $12.5b^3$  to  $8.1b^3$  for  $d = 44 \text{ nm}$ , and from  $14.6b^3$  to  $4.5b^3$  for  $d = 38 \text{ nm}$ ) for strain rates below  $10^{-4} \text{ s}^{-1}$ , concluding that a change in governing plastic deformation mechanisms occurs around that strain rate. Based on their  $V_a$  values, they argue that the controlling mechanisms may shift from intragranular based plasticity at strain rates above  $10^{-4} \text{ s}^{-1}$ , controlled by dislocation nucleation and pinning/depinning from grain boundaries, to grain boundary diffusion and grain boundary sliding mediated by dislocation activity for strain rates below  $10^{-4} \text{ s}^{-1}$ . They repeated these measurements on annealed Au thin films with a larger  $d = 64 \text{ nm}$ , and obtained a bilinear trend as well, from  $V_a = 19.7b^3$  above  $10^{-4} \text{ s}^{-1}$  to  $6.4b^3$  below that strain rate.<sup>57</sup> A direct comparison with our ufg Au films is not straightforward, given the large difference in grain size ( $\sim 50$  vs.  $150 \text{ nm}$ , with grains as large as  $200\text{--}300 \text{ nm}$  in our films). In fact, most of our *in situ* TEM observations of plastic deformation occur for the larger grains, which is normal given that these grains yield first based on the Hall–Petch effect. However, we note that our *in situ* TEM observations, performed in the  $10^{-4}\text{--}10^{-5} \text{ s}^{-1}$  regime, reveal a more complex mechanistic picture than what can be inferred from an activation volume value, with instances of both intragranular dislocation activities controlled by pinning/depinning at GBs (see movies in the ESI† and Fig. 8–10) and intergranular dislocation activities (also observed previously for the same Au films<sup>30</sup>). Hence, we argue that, while measuring a change in activation volume is a strong indication of a change in governing mechanism (especially when measuring  $V^*$  compared to  $V_a$  in order to rule out the effect of mobile dislocation density on the deformation response), concurrent *in situ* TEM observations can greatly help to accurately interpret the change in activation volume values.

Lastly, while we demonstrated our technique for ufg microstructures, other microstructures that have already been fabricated in microspecimen form can also be characterized, including mono-,<sup>58</sup> bi-,<sup>59</sup> and nano-crystalline<sup>60</sup> metals. Single-

crystal microspecimens could be employed to study the deformation kinetics of dislocation/dislocation mechanisms in confined volumes, while bi-crystal specimens would allow careful GB/dislocation interactions for well characterized GBs. Similarly, nc specimens, with much smaller grain sizes than our Au specimens, would enable further investigation of the effect of grain size on these defect mechanics.

## 4. Conclusions

In conclusion, we demonstrated a technique to perform *in situ* TEM measurements of true activation volume on microspecimens, relying on the miniaturization of repeated stress relaxation experiments inside a TEM. The stability of the MEMS device enables accurate measurements of the stress decrease during short relaxation segments, with 1–2 MPa precision, which is shown to be enough to measure  $V^*$  of  $3-5b^3$  in ufg Au specimens. A range of *in situ* TEM observations of grain boundary-dislocation interactions was made during and shortly after the  $V^*$  measurements. The ability to simultaneously observe mechanisms and measure  $V^*$  is expected to provide enhanced integration with atomistic reaction pathway simulations, whereby the *in situ* TEM observations can be reproduced *via* atomistic simulations, and the calculated  $V^*$  can be compared to the measured values.

## Conflicts of interest

There are no conflicts to declare.

## Acknowledgements

SG, SS, TZ, JK and OP gratefully acknowledge support by the U.S. Department of Energy (DOE), Office of Science, Basic Energy Sciences (BES) Materials Science and Engineering (MSE) Division under award #DE-SC0018960. BLB was also funded from the U.S. Department of Energy (DOE), Office of Science, Basic Energy Sciences (BES) Materials Science and Engineering (MSE) Division. This work was performed, in part, at the Center for Integrated Nanotechnologies, an Office of Science User Facility operated for the U.S. Department of Energy (DOE) Office of Science. Sandia National Laboratories is a multimission laboratory managed and operated by National Technology & Engineering Solutions of Sandia, LLC, a wholly owned subsidiary of Honeywell International, Inc., for the U.S. DOE's National Nuclear Security Administration under contract DE-NA-0003525. The views expressed in the article do not necessarily represent the views of the U.S. DOE or the United States Government.

## References

- 1 H. Lim, M. G. Lee, J. H. Kim, B. L. Adams and R. H. Wagoner, *Int. J. Plast.*, 2011, **27**, 1328–1354.
- 2 D. E. Spearot and M. D. Sangid, *Curr. Opin. Solid State Mater. Sci.*, 2014, **18**, 188–195.
- 3 J. Kacher, B. P. Eftink, B. Cui and I. M. Robertson, *Curr. Opin. Solid State Mater. Sci.*, 2014, **18**, 227–243.
- 4 T. Zhu and J. Li, *Prog. Mater. Sci.*, 2010, **55**, 710–757.
- 5 Y. M. Wang, A. V. Hamza and E. Ma, *Acta Mater.*, 2006, **54**, 2715–2726.
- 6 M. A. Meyers, A. Mishra and D. J. Benson, *Prog. Mater. Sci.*, 2006, **51**, 427–556.
- 7 C. Suryanarayana and C. C. Koch, *Hyperfine Interact.*, 2000, **130**, 5–44.
- 8 R. J. Asaro and S. Suresh, *Acta Mater.*, 2005, **53**, 3369–3382.
- 9 K. S. Kumar, H. Van Swygenhoven and S. Suresh, *Acta Mater.*, 2003, **51**, 5743–5774.
- 10 H. Van Swygenhoven, P. M. Derlet and A. G. Froseth, *Nat. Mater.*, 2004, **3**, 399–403.
- 11 H. Van Swygenhoven, P. M. Derlet and A. G. Froseth, *Acta Mater.*, 2006, **54**, 1975–1983.
- 12 A. Rajabzadeh, F. Momprou, M. Legros and N. Combe, *Phys. Rev. Lett.*, 2013, **110**, 265507.
- 13 N. Combe, F. Momprou and M. Legros, *Phys. Rev. B*, 2016, **93**, 024109.
- 14 K. T. Chen, J. Han, S. L. Thomas and D. J. Srolovitz, *Acta Mater.*, 2019, **167**, 241–247.
- 15 J. Han, S. L. Thomas and D. J. Srolovitz, *Prog. Mater. Sci.*, 2018, **98**, 386–476.
- 16 S. L. Thomas, C. Z. Wei, J. Han, Y. Xiang and D. J. Srolovitz, *Proc. Natl. Acad. Sci. U. S. A.*, 2019, **116**, 8756–8765.
- 17 J. W. Cahn, Y. Mishin and A. Suzuki, *Acta Mater.*, 2006, **54**, 4953–4975.
- 18 S. L. Thomas, K. T. Chen, J. Han, P. K. Purohit and D. J. Srolovitz, *Nat. Commun.*, 2017, **8**, 1764.
- 19 D. V. Bachurin, D. Weygand and P. Gumbsch, *Acta Mater.*, 2010, **58**, 5232–5241.
- 20 M. Aramfard and C. Deng, *Modell. Simul. Mater. Sci. Eng.*, 2014, **22**, 055012.
- 21 P. Wang, X. H. Yang and D. Peng, *Comput. Mater. Sci.*, 2016, **112**, 289–296.
- 22 A. Rajabzadeh, M. Legros, N. Combe, F. Momprou and D. A. Molodov, *Philos. Mag.*, 2013, **93**, 1299–1316.
- 23 A. Rajabzadeh, F. Momprou, S. Lartigue-Korinek, N. Combe, M. Legros and D. A. Molodov, *Acta Mater.*, 2014, **77**, 223–235.
- 24 H. A. Khater, A. Serra, R. C. Pond and J. P. Hirth, *Acta Mater.*, 2012, **60**, 2007–2020.
- 25 D. Farkas, S. Mohanty and J. Monk, *Mater. Sci. Eng., A*, 2008, **493**, 33–40.
- 26 J. Kacher, C. Kirchlechner, J. Michler, E. Polatidis, R. Schwaiger, H. Van Swygenhoven, M. Taheri and M. Legros, *MRS Bull.*, 2019, **44**, 465–470.
- 27 E. Spiecker, S. H. Oh, Z.-W. Shan, Y. Ikuhara and S. X. Mao, *MRS Bull.*, 2019, **44**, 443–449.
- 28 S. Bhowmick, H. Espinosa, K. Jungjohann, T. Pardo and O. Pierron, *MRS Bull.*, 2019, **44**, 487–493.
- 29 Q. Yu, M. Legros and A. M. Minor, *MRS Bull.*, 2015, **40**, 62–68.



- 30 E. Hosseinian, M. Legros and O. N. Pierron, *Nanoscale*, 2016, **8**, 9234–9244.
- 31 E. Hosseinian and O. Pierron, *Nanoscale*, 2013, **5**, 12532–12541.
- 32 P. F. Rottmann and K. J. Hemker, *Acta Mater.*, 2017, **140**, 46–55.
- 33 F. Mompou and M. Legros, *Scr. Mater.*, 2015, **99**, 5–8.
- 34 H. Idrissi, A. Kobler, B. Amin-Ahmadi, M. Coulombier, M. Galceran, J. P. Raskin, S. Godet, C. Kubel, T. Pardoën and D. Schryvers, *Appl. Phys. Lett.*, 2014, **104**, 101903.
- 35 J. Kacher, T. Zhu, O. Pierron and D. E. Spearot, *Curr. Opin. Solid State Mater. Sci.*, 2019, **23**, 117–128.
- 36 P. Spätig, J. Bonneville and J. L. Martin, *Mater. Sci. Eng., A*, 1993, **167**, 73–79.
- 37 D. Caillard and J. Martin, *Thermally Activated Mechanisms in Crystal Plasticity*, Pergamon Materials Series, 2003.
- 38 L. Lu, T. Zhu, Y. Shen, M. Dao, K. Lu and S. Suresh, *Acta Mater.*, 2009, **57**, 5165–5173.
- 39 Y. M. Wang, A. V. Hamza and E. Ma, *Appl. Phys. Lett.*, 2005, **86**, 241917.
- 40 S. Gupta and O. Pierron, *J. Microelectromech. Syst.*, 2017, **26**, 1082–1092.
- 41 G. Mohanty, J. Wehrs, B. L. Boyce, A. Taylor, M. Hasegawa, L. Philippe and J. Michler, *J. Mater. Res.*, 2016, **31**, 1085–1095.
- 42 B. Merle, *J. Mater. Res.*, 2019, **34**, 69–77.
- 43 T. Zhu, J. Li, A. Samanta, H. G. Kim and S. Suresh, *Proc. Natl. Acad. Sci. U. S. A.*, 2007, **104**, 3031–3036.
- 44 D. K. Chen, L. L. Costello, C. B. Geller, T. Zhu and D. L. McDowell, *Acta Mater.*, 2019, **168**, 436–447.
- 45 B. Pant, B. L. Allen, T. Zhu, K. Gall and O. N. Pierron, *Appl. Phys. Lett.*, 2011, **98**, 053506.
- 46 B. Pant, S. Choi, E. Baumert, B. Allen, S. Graham, K. Gall and O. Pierron, *Exp. Mech.*, 2012, **52**, 607–617.
- 47 S. Gupta and O. N. Pierron, *Extreme Mech. Lett.*, 2016, **8**, 167–176.
- 48 J. L. Martin, B. Lo Piccolo, T. Kruml and J. Bonneville, *Mater. Sci. Eng., A*, 2002, **322**, 118–125.
- 49 L. Lu, M. Dao, T. Zhu and J. Li, *Scr. Mater.*, 2009, **60**, 1062–1066.
- 50 N. Mortazavi, M. Esmaily and M. Halvarsson, *Mater. Lett.*, 2015, **147**, 42–45.
- 51 L. Wang and B. C. Prorok, *J. Mater. Res.*, 2008, **23**, 55–65.
- 52 K. Jonnalagadda, N. Karanjaokaar, I. Chasiotis, J. Chee and D. Peroulis, *Acta Mater.*, 2010, **58**, 4674–4684.
- 53 M. Dupraz, Z. Sun, C. Brandl and H. Van Swygenhoven, *Acta Mater.*, 2018, **144**, 68–79.
- 54 S. H. Li, W. Z. Han and Z. W. Shan, *Acta Mater.*, 2017, **141**, 183–192.
- 55 R. Sarkar, C. Rentenberger and J. Rajagopalan, *Sci. Rep.*, 2015, **5**, 16345.
- 56 B. Merle, D. Cassel and M. Goken, *J. Mater. Res.*, 2015, **30**, 2161–2169.
- 57 N. J. Karanjaokaar, C. S. Oh, J. Lambros and I. Chasiotis, *Acta Mater.*, 2012, **60**, 5352–5361.
- 58 V. Samaee, R. Gatti, B. Devincre, T. Pardoën, D. Schryvers and H. Idrissi, *Sci. Rep.*, 2018, **8**, 12012.
- 59 J. P. Liebig, M. Göken, G. Richter, M. Mačković, T. Przybilla, E. Spiecker, O. N. Pierron and B. Merle, *Ultramicroscopy*, 2016, **171**, 82–88.
- 60 M. S. Colla, B. Amin-Ahmadi, H. Idrissi, L. Malet, S. Godet, J. P. Raskin, D. Schryvers and T. Pardoën, *Nat. Commun.*, 2015, **6**, 5922.